NeuroImage 70 (2013) 308–316

Contents lists available at SciVerse ScienceDirect

NeuroImage

journal homepage: www.elsevier.com/locate/ynimg

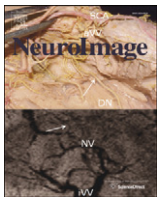

Improvement of the SNR and resolution of susceptibility-weighted venography by model-based multi-echo denoising

Ung Jang, Yoonho Nam, Dong-Hyun Kim, Dosik Hwang *

School of Electrical and Electronic Engineering, College of Engineering, Yonsei University, 262 Seongsanno, Seodaemun-gu, Seoul 120-749, Republic of Korea

ARTICLE INFO

Article history:
Accepted 28 December 2012
Available online 5 January 2013

Keywords:
Venography
Susceptibility weighted imaging
T2* relaxation
Model-based denoising
Multi-echo MR data

ABSTRACT

The vein structures of the brain are important for understanding brain function and structure, especially when functional magnetic resonance imaging (fMRI) is utilized, as fMRI is based on changes in the blood-oxygen-level-dependent (BOLD) signal, which is directly related to veins. The aim of the present study was to develop an effective method to produce high signal-to-noise-ratio (SNR) and high-resolution multi-contrast susceptibility-weighted (SW) images of vein structures from 3 T magnetic resonance (MR) scanners using multi-gradient-echo MR acquisition and a successive denoising process for both magnitude and phase data. Successive multi-echo MR images were acquired at multiple time points using a multigradient-recalled echo sequence at 3 T, and noise in the magnitude and phase data was effectively suppressed using model-based denoising methods. A T_2^* relaxation model was used to denoise the magnitude data and a linear phase model was used to denoise the phase data. SW venography images were obtained from the denoised MR data and compared with conventional SW venography. To evaluate the performance of our denoising methods, we conducted numerical simulation studies and compared the mean-squared-error (MSE), SNR, and contrast-to-noise ratio (CNR) that we obtained using our procedure with those obtained using conventional denoising methods. In addition, images were inspected visually. Numerical simulations showed that our proposed model-based denoising methods were the most effective at suppressing noise. In vivo experiments also showed a substantial increase in the SNR of the phase mask obtained using the proposed denoising process (twice that of the conventional GRE-based phase mask). The T_2^* relaxation model method improved the SNR of the magnitude image (1.17–1.35 times that of the GRE-based magnitude image). Noise suppression of both magnitude and phase data using our proposed method resulted in an overall increase in the SNR and CNR in the final SW venography (1.1–1.5-fold and 1.96-fold higher SNR and CNR, respectively, than that of the GRE-based SW venography). We demonstrated that high SNR and high-resolution SW venograms can be obtained using multi-echo gradient-recalled acquisition and successive model-based denoising of both magnitude and phase data.

Introduction

Vein structures in the brain are important for understanding brain function, especially when functional magnetic resonance imaging (fMRI) is utilized, as fMRI is based on changes in the blood-oxygen-level-dependent (BOLD) signal, which is related to veins. MR venography, which is the imaging of vein structures using MRI, has recently gained attention in the diagnosis of vascular diseases, because MRI does not result in exposure of the patient to ionizing radiation, unlike X-rays or computed tomography (CT). Good venography should image as many veins as possible, including veins with diameters of 10 to 100 μm such as venules, precapillary sphincters, arterioles, small pial veins, and even much smaller veins such as capillaries (Berne and Levy, 1988). The diameter of a vein influences blood flow in that the speed of the blood flow is proportional to the reciprocal of the cross-sectional area of a vein. The speed of blood flow in small veins such as capillaries can be as fast as 0.5–3 mm/s (Pawlik et al., 1981). Therefore, techniques that depend on the speed of blood flow, such as time-of-flight angiography or phase contrast angiography, have difficulty imaging small veins (Potchen et al., 1993). In contrast, BOLD-based venography, which utilizes the susceptibility difference between oxygenated and deoxygenated hemoglobin using a gradient-recalled-echo (GRE) pulse sequence, can detect small veins without reference to the speed of blood flow (Hoogenraad et al., 1998; Ogawa et al., 1990; Reichenbach et al., 2000). Veins and the surrounding tissues have different susceptibilities, thus leading to different phases in MR signals, which can be utilized to enhance vein contrast in venography. This technique, called susceptibility-weighted imaging (SWI), has been extensively investigated in recent years and has been used for efficient venography (Haacke et al., 2004, 2009; Jin et al., 2008; Kiselev and Posse, 1999; Xu and Haacke, 2006). However, although substantial improvements in SW venography have been made, there are several issues that still require improvement.

The first issue is resolution. As mentioned earlier, the diameter of veins can range from a few μm to a few hundred μm. However, to

* Corresponding author. Fax: +82 2 313 2879.
E-mail address: dosik.hwang@yonsei.ac.kr (D. Hwang).

1053-8119/$ – see front matter © 2013 Elsevier Inc. All rights reserved.
http://dx.doi.org/10.1016/j.neuroimage.2012.12.067

date, the maximum reported in-plane resolution of SW venography is 0.5×0.5 mm^2 at 3 T (Haacke et al., 2009). Therefore, conventional SW venographies cannot resolve small veins such as venules, precapillary sphincters, arterioles, or capillaries. To resolve these small veins, the image resolution has to be increased. However, this may lead to a decrease in the SNR of venography performed using conventional settings. Therefore, novel methods need to be developed to either increase resolution without compromising the SNR or to restore the reduced SNR in high-resolution SW venography through use of post-processing methods. The conventional post-processing approach taken to increase SNR and reduce noise in images is to use spatial filters such as a Gaussian low-pass filter (LPF) (Wink and Roderick, 2004), a median filter (MF) (Ying et al., 1996), or an anisotropic diffusion filter (ADF) (Samsonov and Johnson, 2004). These filters are very effective at suppressing noise, but they tend to remove detailed information such as edges between tissues, fine structures, and small veins, or induce artificial features such as staircasing artifacts or artificial patches due to nonlinear processing (Samsonov and Johnson, 2004; Wink and Roderick, 2004; Ying et al., 1996). These artifacts can be detrimental to accurate diagnoses in the clinical setting. Therefore, an effective post-processing technique that can increase spatial resolution in SW venography while compensating for the reduction in the SNR without introducing artifacts should be developed.

The second issue is that the optimal echo time (TE) to produce a high-contrast image of veins varies depending on the orientation of the veins. It has been reported that veins parallel to the static field have optimal contrast at TE = 28 ms, while other veins may require later echoes (Haacke et al., 2004; Hernando et al., 2012; Reichenbach et al., 2000), suggesting that there are difficulties in imaging all types of veins in a single venography at a fixed TE. Furthermore, the use of later echoes to depict veins that are not parallel to the static field results in a substantial reduction in the SNR, which degrades the overall quality of SW venography. In this case, post-processing techniques to effectively suppress noise that do not introduce spatial artifacts are required.

Jang and Hwang (2012) proposed an effective post-processing method to increase the SNR without introducing spatial artifacts for successive multi-echo MR images acquired at multiple time points. They showed that high-quality multiple T_2* contrast images can be effectively obtained by suppressing noise from low-quality multi-echo images in the magnitude data (Jang and Hwang, 2012). This technique could potentially improve the quality of SW venography, where multiple images are necessary to depict various veins while retaining high resolution and a high SNR. Therefore, in this paper, we extend this method to include phase data for susceptibility-weighting, and propose a new method to generate high-resolution and high-SNR multiple SW venography images using a T_2* relaxation model for noise suppression in the multi-echo magnitude data and a linear phase model for noise suppression in the multi-echo phase data used for susceptibility-weighting.

Methods

Data acquisition

For in vivo experiments, normal volunteers were scanned with a conventional GRE sequence and a multi-gradient echo (MGRE) sequence using a 3 T Siemens MRI system (Erlangen, Germany). The GRE sequence parameters were a repetition time (TR) of 30 ms, TE of 20 ms, flip angle of 12°, field of view (FOV) of 215×215 mm^2, acquisition matrix of 512×512, slice thickness of 1.6 mm, and bandwidth of 80 Hz/Px. These parameters were selected based on the conventional SWI GRE sequence (Haacke et al., 2009). The only difference in our sequence was that the FOV was slightly reduced to maximize in-plane resolution and the slice thickness was changed from 1.4 mm to 1.6 mm. To further increase in-plane resolution, 512×512 images were interpolated into 1024×1024 images, resulting in an effective resolution of 0.21×0.21 mm^2. MGRE sequence parameters were a TR of 95 ms, TE1 of 5.67 ms, echo spacing (ES) of 5.51 ms, flip angle of 27°, FOV of 215×215 mm^2, acquisition matrix of 512×512 (interpolated to 1024×1024), slice thickness of 1.6 mm, bandwidth of 444 Hz/Px, and acquisition of 16 echoes. Generalized autocalibrating partially parallel acquisition (GRAPPA) (Griswold et al., 2002) was applied to multi-echo sequences to reduce the total acquisition time by half. The total acquisition time for MGRE imaging was 15 min 30 s. For comparison with conventional GRE imaging, the 4th TE at 22.2 ms was selected, which is comparable to a TE of 20 ms in GRE imaging. A repetition of two was used in conventional GRE imaging to improve the SNR and to achieve a similar acquisition time as that required for the proposed MGRE imaging. Therefore, the total acquisition time for GRE imaging was 17 min, which was even longer than that of MGRE imaging. Multiple SW venographies obtained from the in vivo data using the proposed MGRE method were compared with conventional SW venographies to determine if our proposed multi-echo SW venography method could effectively generate high-resolution and high-SNR multiple venographies. This study was approved by the Institutional Review Board of our hospital, and written informed consent was obtained from all subjects.

Denoising of magnitude data in the temporal domain: T_2 relaxation model-based approach*

Multiple images were obtained at multiple time points using the MGRE sequence. These multi-echo images were arranged in time so that each voxel had its own decay signal in the temporal domain. Noise in magnitude data can be reduced effectively by using a model-based denoising method (Jang and Hwang, 2011, 2012). In this method, the decay signal is fitted to a T_2* relaxation model on a voxel-by-voxel basis, and noise is substantially suppressed during the fitting process. The fitting process is performed voxel-by-voxel, independently of neighboring voxels, and therefore there is no interference between voxels and none of the spatial artifacts that are often observed in conventional spatial filters (Jang and Hwang, 2012). The T_2* relaxation curves of most brain tissues such as white matter and gray matter follow a multi-exponential decay pattern (Andrews et al., 2005; Hwang and Du, 2009; Jang and Hwang, 2012; Lancaster et al., 2003; Valentine et al., 2007; Wachowicz and Snyder, 2002). Therefore, we used a multi-exponential decay model for the fitting process. The non-negative least squares (NNLS) algorithm was used for fitting (Lawson and Hanson, 1974; Provencher, 1982).

The T_2* relaxation model-based denoising method can be applied to general regions in multi-echo MR magnitude images. However, regions with severe field inhomogeneity and susceptibility differences, such as veins, cannot be completely resolved using the T_2* relaxation multi-exponential model (Reichenbach et al., 1997). Vein contrast might not be adequately expressed in the final venography images if the same T_2* relaxation model is used to fit the non-exponential rapid decay signals, due to the susceptibility difference in veins. Therefore, another model is needed to denoise the non-exponential decay signals from veins. Based on simple simulation studies, we determined that a piecewise polynomial model (Fan and Gijbels, 1996) is an effective model to fit non-exponential decay signals. In this piecewise polynomial model, the decay signals are segmented into several pieces, and those segmented signals are fitted using polynomial functions. We applied the piecewise polynomial model when fitting with the NNLS model resulted in a high fitting error over a certain threshold. Use of this fitting process in the temporal domain effectively suppressed the noise in the magnitude data in the spatial domain. We applied this model-based denoising method using the T_2* relaxation model and piecewise polynomial model to the in vivo data and achieved effective noise suppression. The fitted (denoised) images were used to generate the final SW venographies.

Denoising of phase data in the temporal domain: linear phase model-based approach

Noise in the phase data in a multi-echo MR dataset can be effectively reduced in a similar manner to noise suppression of the magnitude data. We performed phase unwrapping in the temporal domain, and then applied model-based denoising to the unwrapped phase data. The phase data at long TE, when the intensity of the magnitude data decreased below the noise level, were not included in the fitting process.

Phase evolution in the temporal domain can be described by the following equation (Haacke et al., 2009):

$$\Delta\Phi = -\gamma\cdot\Delta B\cdot TE \tag{1}$$

where γ is the gyromagnetic ratio (2π*42.58 MHz/T), ΔB is the field gradient due to field inhomogeneity, and TE is the echo time. When ΔB is fixed, the phase varies following a first order linear model. Therefore, the linear phase model shown in Eq. (2) was used to suppress the noise in the phase data of the multi-echo dataset acquired in the present study as follows:

$$\Phi(TE) = \phi TE + \phi_0 \tag{2}$$

where ϕ is the rate of phase change with time and ϕ_0 is the phase at TE = 0 ms. The phase data were fitted with model Eq. (2) using a least squares (LS) algorithm (Abdi, 2003). The LS algorithm estimates the unknown parameters ϕ and ϕ_0 so that the LS error between the phase data and the model is minimized, as expressed in Eq. (3):

$$\min_{s} ||As-y||_2^2 \tag{3}$$

where y is the acquired phase signal and s is the unknown coefficient of Eq. (2), ϕ and ϕ_0. A is the linear operator which transforms the unknown values s into the acquired phase signal y ($y = A\cdot s$).

We applied the linear phase model-based denoising method to synthetic data in simulation studies and in vivo data, and compared its denoising performance with that of conventional filtering methods.

Generation of synthetic phase data

We used complex MR datasets emulating brain tissues to evaluate the performance of our proposed denoising procedure. Fig. 1(a) shows the phase image of a single slice at TE = 20 ms. Brain tissues consist of white matter, gray matter, and cerebrospinal fluid (CSF). Complex multi-echo MR datasets for these three regions were generated using Eqs. (4a),(4b),(4c) by considering their decay characteristics. The image matrix size was 128×128, TE1 was 3 ms, ES was 1 ms, and the total number of echoes was 60. Decay characteristics were based on multi-compartmental models (Andrews et al., 2005; Hwang and Du, 2009; Lancaster et al., 2003; Valentine et al., 2007; Wachowicz and Snyder, 2002). Normal white matter has three different water pools with relaxation times of 15, 35, and 60 ms (4a), which represent the water pools of myelin, axons, and intra/extra-cellular spaces, respectively (Hwang et al., 2010; Lancaster et al., 2003). Normal gray matter has little myelin, thus, the first component in Eq. (4a) was removed in Eq. (4b) for gray matter. CSF has a long relaxation time and decays slowly as in Eq. (4c) (Hwang and Du, 2009; Lancaster et al., 2003). The phases for each region were determined from the average phases of the real in vivo MR data.

$$S_{WM}(TE) = \left(1\times e^{-\frac{TE}{15}} + 3\times e^{-\frac{TE}{35}} + 6\times e^{-\frac{TE}{60}}\right)e^{j(0.0795TE-0.0012)}. \tag{4a}$$

$$S_{GM}(TE) = \left(4\times e^{-\frac{TE}{35}} + 6\times e^{-\frac{TE}{60}}\right)e^{j(0.0620TE-0.0224)}. \tag{4b}$$

$$S_{CSF}(TE) = \left(10\times e^{-\frac{TE}{150}}\right)e^{j(0.0863TE-0.1671)}. \tag{4c}$$

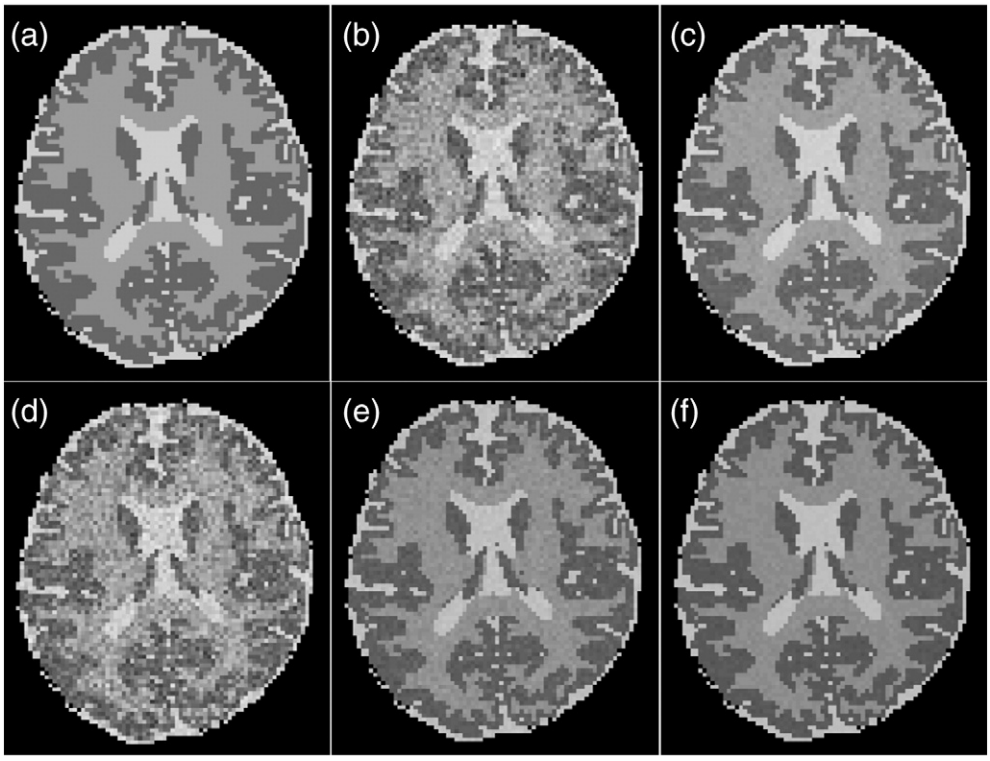

Fig. 1. Comparison of temporally denoised phase image at TE = 20 ms. Conventional filters and the linear phase model-based method were applied to the synthetic dataset in the temporal domain. True image (a), noisy image with SNR = 4.5 (b), and images denoised by temporal filtering with LPF (c), MF (d), ADF (e), and the model-based method using a linear phase model (f).

Gaussian random noise was added to the real and imaginary parts individually to generate noisy MR signals. The SNR of the noisy simulation data was 4.5 at the first TE.

Comparison and evaluation of denoising performance

We compared the performance of our proposed linear phase model-based denoising method with that of conventional filters applied to the temporal domain (decay signals). The phase data in the temporal domain was denoised using a Gaussian low-pass filter (LPF), a median filter (MF), and an anisotropic diffusion filter (ADF). Parameters for these filters were selected by evaluating the mean square error (MSE) between the true phase image and the denoised images to allow the filter parameters to produce the minimum MSE. The standard deviation of the Gaussian function and the kernel length of the LPF was 20 and 7 samples, respectively. The kernel size of MF was 3, κ for ADF was 30.5, and the number of iterations was 30 (κ is the flow constant and controls how strongly the diffusion process will be induced during ADF filtering (Gerig et al., 1992; Samsonov and Johnson, 2004)).

Finally, the performance of the proposed SW venographies using MGRE and successive model-based denoising methods was compared with that of conventional SW venographies obtained using the GRE imaging. The phase masks were multiplied four times with the magnitude images to produce SW venographies (Haacke et al., 2009). The denoising performance was evaluated qualitatively by visual comparison and quantitatively by CNR comparison. CNR was defined as follows:

$$CNR_{ab} = |S_a - S_b|/\sigma_b \quad (5)$$

where S_a and S_b are the mean signal intensities in area 'a' and area 'b', respectively, and σ_b is the standard deviation of the signal intensities in area 'b'.

The numerical data had clear boundaries among different tissues so that the regions of interest (ROIs) for the CNR calculation, namely a and b, could be determined unambiguously. However, in vivo data have rather smooth boundaries between different tissues, and accurate calculation of CNR is difficult. Furthermore, the ROIs in the present study were veins, which are thin and long, and therefore determination of the ROIs and the background was not straightforward. To address this, we defined a line-based contrast-to-noise ratio (LB-CNR) to evaluate the CNR of the SW venographies. The equation used to calculate the CNR is the same as Eq. (5), but the ROI and background area were defined as the set of pixels describing curved lines, such as veins, as shown in Fig. 2. The mean signal intensities of a vein and its background were calculated from the pixels on the solid line and dashed line, respectively.

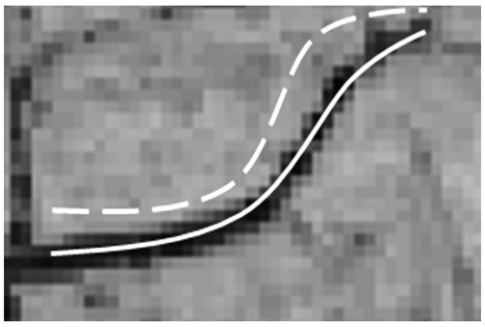

Fig. 2. Description of line-based (LB) CNR for in vivo blood vessels. The ROI for the vein was defined as the set of pixels on the curved line passing through the center of the vein. The background was defined as the set of pixels on the curved dashed line surrounding the vein. LB-CNR was calculated based on the two LB ROIs.

Results

Fig. 1 shows the true phase image (a), the noisy image (b) from the synthetic dataset at TE = 20 ms, images denoised by temporal filtering with LPF (c), MF (d), ADF (e), and the results obtained after applying our proposed linear phase model-based method (f) to the temporal domain. The denoising process was performed independently in the temporal domain in a voxel-by-voxel manner, and therefore no spatial artifacts such as blurring, artificial patches, or staircasing artifacts were observed. The proposed method showed the best denoising performance. The MSEs were calculated as 0.0864, 0.0255, 0.0927, 0.0333, 0.0141 for the original noisy image, images denoised with LPF, MF, ADF, and the model-based method, respectively. LPF showed the second-best performance. Because unwrapped phase data varies linearly with time, true phase variation is mostly in the low-frequency range, and therefore high-frequency noise can be effectively reduced by LPF.

Fig. 3 shows the CNRs of the images in Fig. 1 for further quantitative comparison. The 'reference' is the original noisy image, 'CSF & WM' indicate the CNR when the CSF was the ROI and WM was the background, and 'WM & GM' indicates CNR when the WM was the ROI and GM was the background. This CNR comparison revealed that the proposed linear phase model-based denoising method performed the best of all the methods evaluated, consistent with the visual inspection and MSE results.

The noise reduction in the magnitude data was also most effectively achieved by the model-based denoising method. Fig. 4 shows the magnitude venography without the denoising process (a) and the venography denoised using the T_2^* relaxation model at TE = 22.2 ms (d). Figs. 4(b) and (e) are enlarged images of Figs. 4(a) and (d), respectively. The small veins in Fig. 4(b) were not conspicuous due to the presence of high noise throughout the image. In contrast, substantial noise reduction was observed in tissues and blood veins, increasing the conspicuity of the small veins (see Fig. 4(e)). Figs. 4(c) and (f) show the venography profiles along the solid lines in Figs. 4(b) and (e), respectively. Noisy signal fluctuation was substantially reduced at the tissue region, and vein signals were enhanced. The denoising method based on the T_2^* relaxation model and the piecewise polynomial model effectively reduced noise in the multiple-echo magnitude data.

Fig. 5 shows the phase mask of the in vivo data at TE = 20 ms obtained using GRE imaging (a), MGRE imaging without denoising at TE = 22.2 ms (b), and MGRE imaging with denoising using our proposed linear phase model (c). Figs. 5 (d–f) are magnified inset images of (a–c), respectively. The ideal phase mask for SW venography should have a value of 1 for the non-vein area. The phase mask used for conventional GRE imaging (a) shows good vein structures, but the magnified inset image (d) shows the presence of substantial noise in the non-vein area. This noise was amplified when multiplied with the magnitude image (susceptibility-weighting). The original phase mask from MGRE imaging (b and e) had severe noise in the non-vein area that was worse than the noise in the conventional phase mask (a and d). However, the linear phase model-based denoising method reduced the noise substantially, resulting in an improved phase mask (c and f). Vein structures became more conspicuous than in the conventional GRE-based phase mask because noise in the neighborhood of veins was suppressed. The average SNRs were calculated over the tissue regions in the phase mask for quantitative comparison. SNRs were 42.38, 2.67, 95.49 for the GRE-based phase mask, the MGRE-based phase mask prior to denoising, and the denoised phase mask, respectively. Our proposed denoising process increased the SNR substantially (twice that of the conventional GRE-based phase mask).

Fig. 6(a) shows the SW venography at a TE of 20 ms obtained from our 3 T scanner using the same GRE sequence as described in the review paper by Haacke et al. (2004) (The SW venography of a similar slice to that used in our study is shown in Fig. 8(b) of the review paper.) Fig. 6(b) shows the SW venography at a TE of 22.2 ms obtained from MGRE imaging without denoising. Fig. 6(c) shows the denoised SW

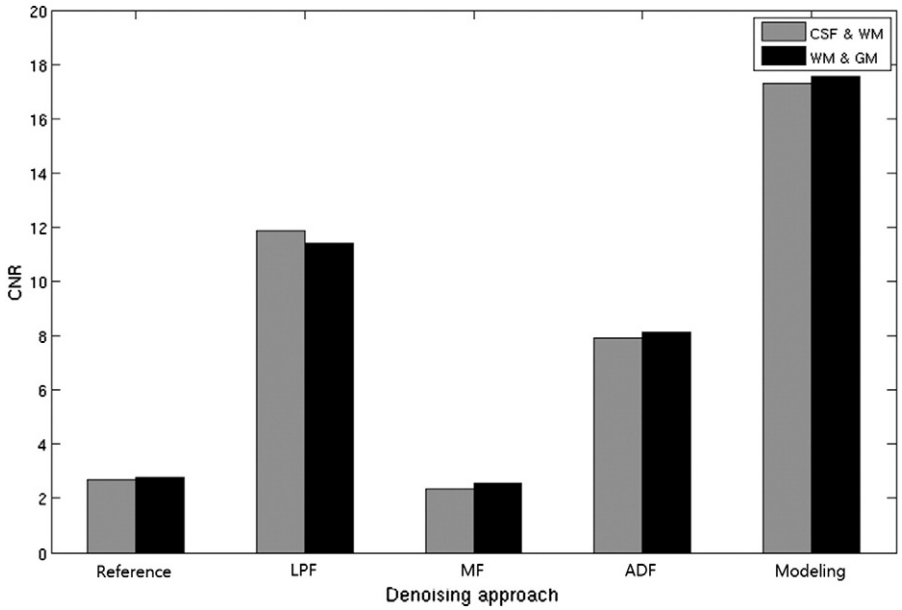

Fig. 3. CNRs of the temporally denoised images shown in Fig. 1. Two CNRs were calculated between CSF & WM, and between WM & GM. The linear phase model-based method resulted in the highest CNRs for all cases.

venography using the proposed method. Data for the GRE and MGRE imaging were acquired so that a similar volume was included. Magnified inset images of the areas surrounded by dotted boxes in Figs. 6(a–c) are shown in Figs. 6(d–f), respectively. The original MGRE SW venography (e) contained a high level of noise, which decreased the conspicuity of small and low-contrast veins. However, the denoised MGRE SW venography (f) showed a substantial reduction in noise and improved vein conspicuity. The contours of the veins were well resolved and the connectivity of the veins was clear. Vein detectability was better in the SW venography denoised using our proposed method than conventional GRE imaging. The veins indicated by white arrows are examples of veins that were difficult to observe in the conventional GRE SW venography (d) but were clearly visible in images obtained using our proposed method (f).

For quantitative comparison, the SNR in several ROIs was calculated for the SW venographies obtained using conventional GRE imaging, MGRE without denoising, and MGRE with denoising. The ROIs included the forceps minor, caudate nucleus, internal capsule, thalamus, optic radiation, and forceps major (Woolsey et al., 2008). In all ROIs, the average SNR increased due to the denoising process (2.27-fold that of the SNR of the original MGRE venography before denoising and 1.1–1.5-fold that of the SNR of the conventional GRE venography (Fig. 7)). For further comparison, CNRs were calculated as LB-CNR in nine veins: the septal vein (SV), transverse caudate vein (TCV), internal

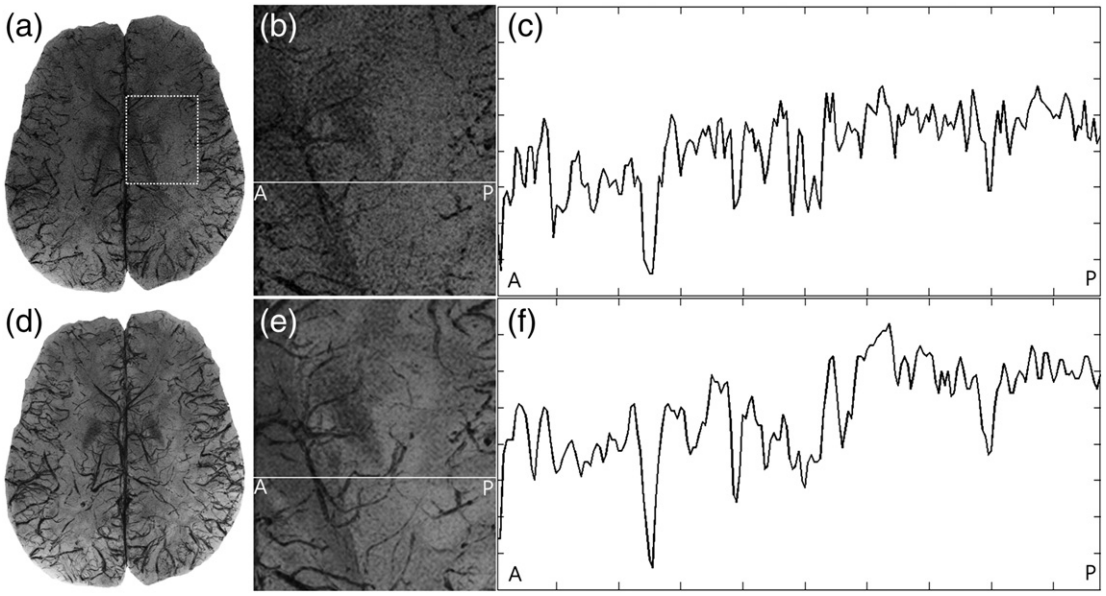

Fig. 4. Comparison of the magnitude venography of the in vivo data acquired by MGRE imaging at TE = 22.2 ms prior to denoising (a) and after denoising using the T_2^* relaxation model and piecewise polynomial model (d). (b) and (e) are magnified inset images of (a) and (d), respectively. (c) and (f) are the line profiles of the white solid line in (b) and (e), respectively.

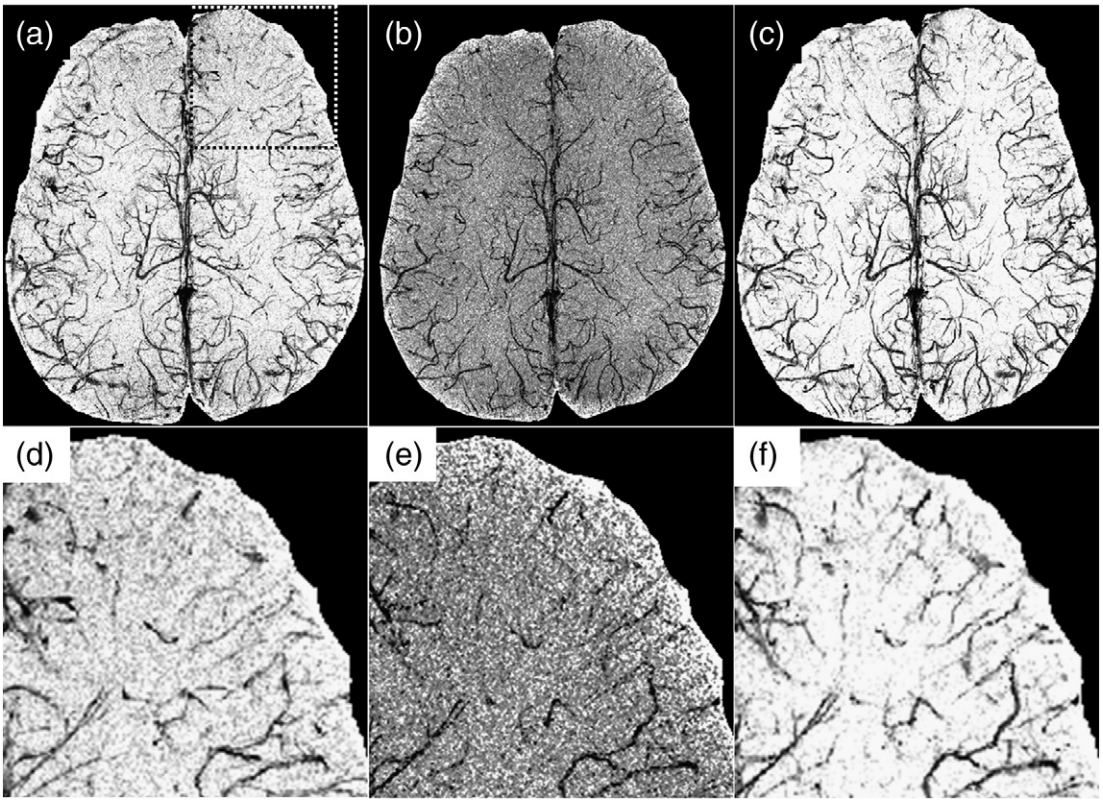

Fig. 5. Comparison of the phase mask of the in vivo data acquired by conventional GRE imaging at TE = 20 ms (a), the original phase mask obtained by MGRE imaging at TE = 22.2 ms (b), and the phase mask denoised using a linear phase model (c). (d–f) are magnified inset images of (a–c), respectively.

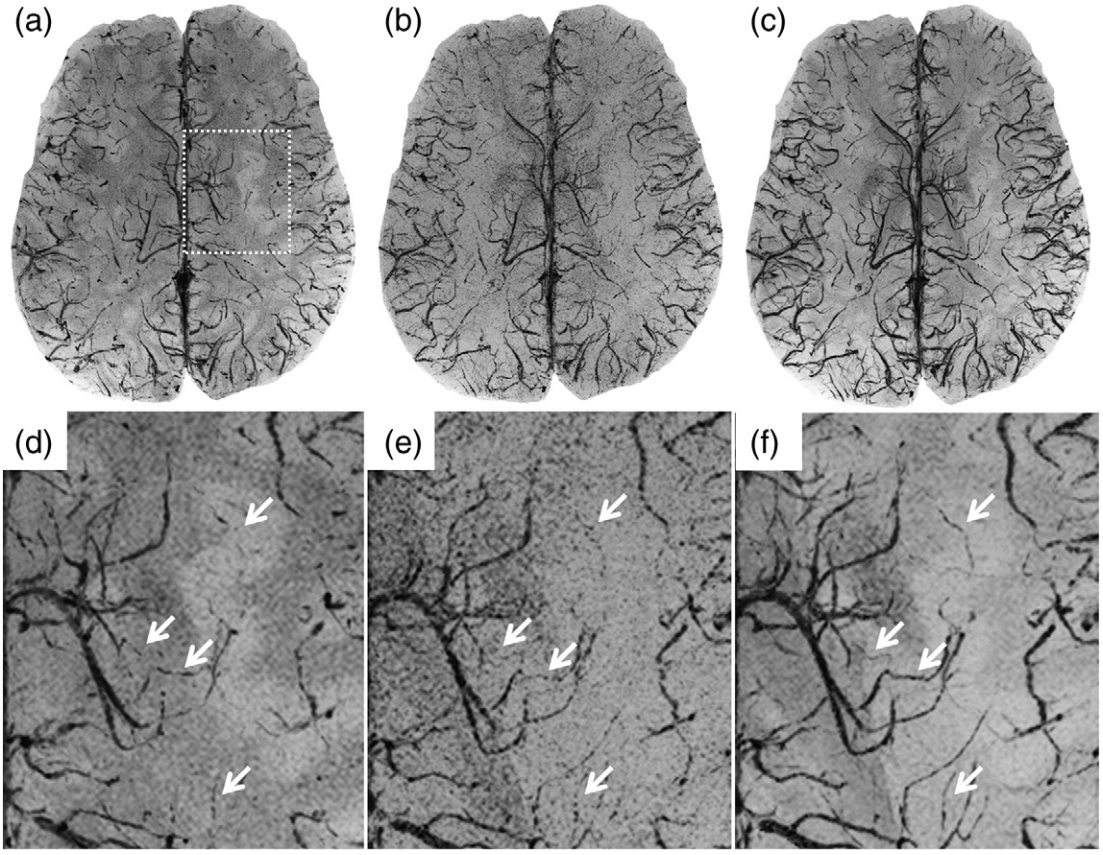

Fig. 6. Comparison of SW venographies. SW venography obtained from conventional GRE imaging at TE = 20 ms (a), noisy SW venography from MGRE imaging at TE = 22.2 ms (b), and denoised SW venography of (b) with two model-based methods (c). (d–f) the magnified images of (a–c), respectively.

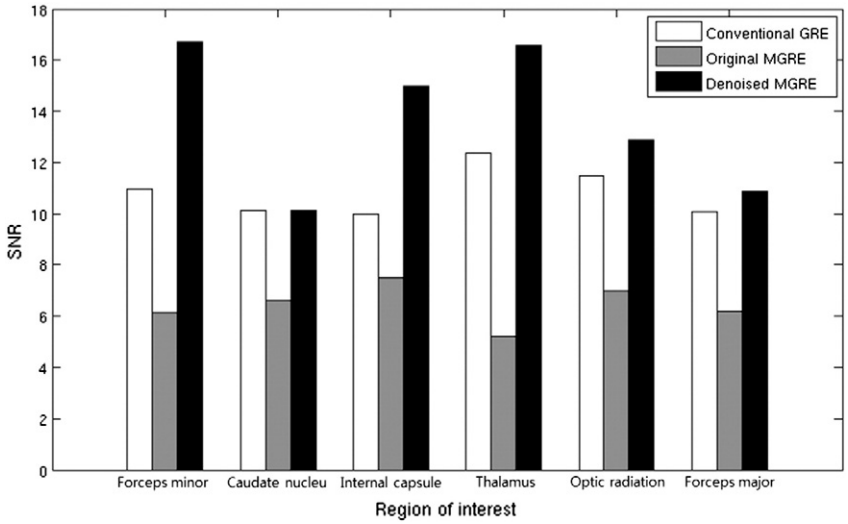

Fig. 7. SNR of (a), (b), (c) of Fig. 6 for six different ROIs. In all cases, the proposed method resulted in the highest SNR.

cerebral vein (ICV), striatal vein (STV), terminal vein (TV), lateral atrial vein (LAV), basal vein (BV), interior capillary, and posterior capillary (Dudink et al., 2008; Rodallec et al., 2006). CNRs were compared among the conventional GRE (Fig. 6a), the original MGRE (Fig. 6b), and the denoised MGRE venographies (Fig. 6c), as shown in Fig. 8. The denoised MGRE venography increased the overall CNR (1.96-fold that of the conventional GRE venography).

Fig. 9 shows three examples of different SW venographies obtained using the proposed method at three different TEs of 11.18 ms (a), 27.71 ms (b), and 44.24 ms (c). Magnified views of the boxed areas are shown in (d)–(f), respectively. In contrast to the conventional GRE-based single SW venography, the proposed method provided multiple-contrast venographies with higher SNR and CNR values than those of conventional single SW venography.

Discussion

We demonstrated that model-based denoising with MGRE data acquisition can produce high-resolution and high-SNR multiple-contrast SW venographies. We used a T_2^* relaxation model to denoise the magnitude data in the temporal domain, and a linear phase model to reduce noise in the phase data. Because the denoising process was performed on a voxel-by-voxel basis in the temporal domain, the denoising process did not introduce any spatial artifacts, such as blurring or artificial features. Simulation studies showed that the linear phase model-based approach outperformed conventional filters, with minimum MSE and maximum CNR values. The same approach was applied to the in vivo phase data, and an improved phase mask was obtained. The SNR of the phase mask obtained using our proposed method was twice the SNR of the conventional GRE phase mask.

Accurate calculation of CNR for in vivo data is difficult because the boundaries of tissues are not clearly defined. If the ROIs for the CNR calculation in Eq. (5) include heterogeneous regions, then σ_b in Eq. (5) may include variations of signal components, rather than only noise components. Therefore, we selected regions that were as homogeneous as possible for CNR calculation.

MGRE-based SW venographies have additional advantages over conventional GRE imaging with respect to the "temporal footprint" (Haider et al., 2008) and multiple contrasts at different TEs. The concept of a temporal footprint was introduced to evaluate the temporal fidelity of

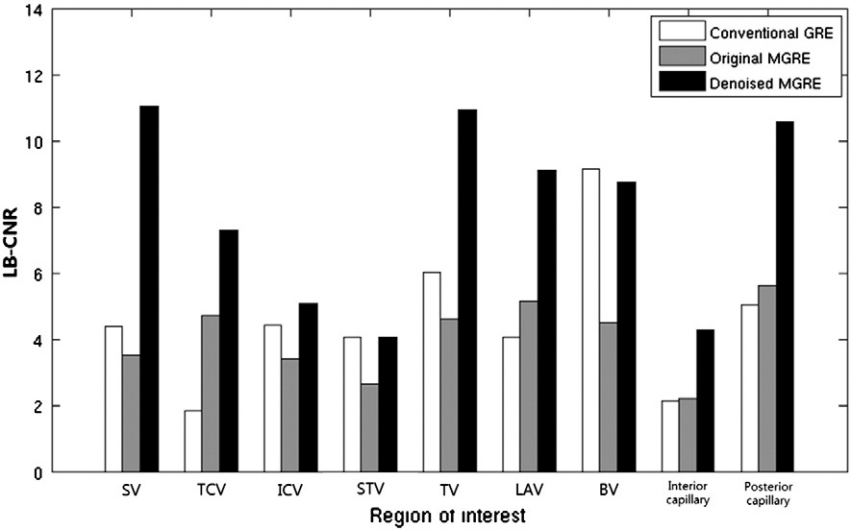

Fig. 8. LB-CNR of (a), (b), (c) of Fig. 6 for nine ROIs (septal vein, SV; transverse caudate vein, TCV; internal cerebral vein, ICV; striatal vein, STV; terminal vein, TV; lateral atrial vein, LAV; basal vein, BV). The proposed method resulted in the highest CNR for most ROIs, except STV and BV. The overall CNR of venographies obtained using our proposed method was 1.9-fold higher than that of conventional GRE-based SW venography.

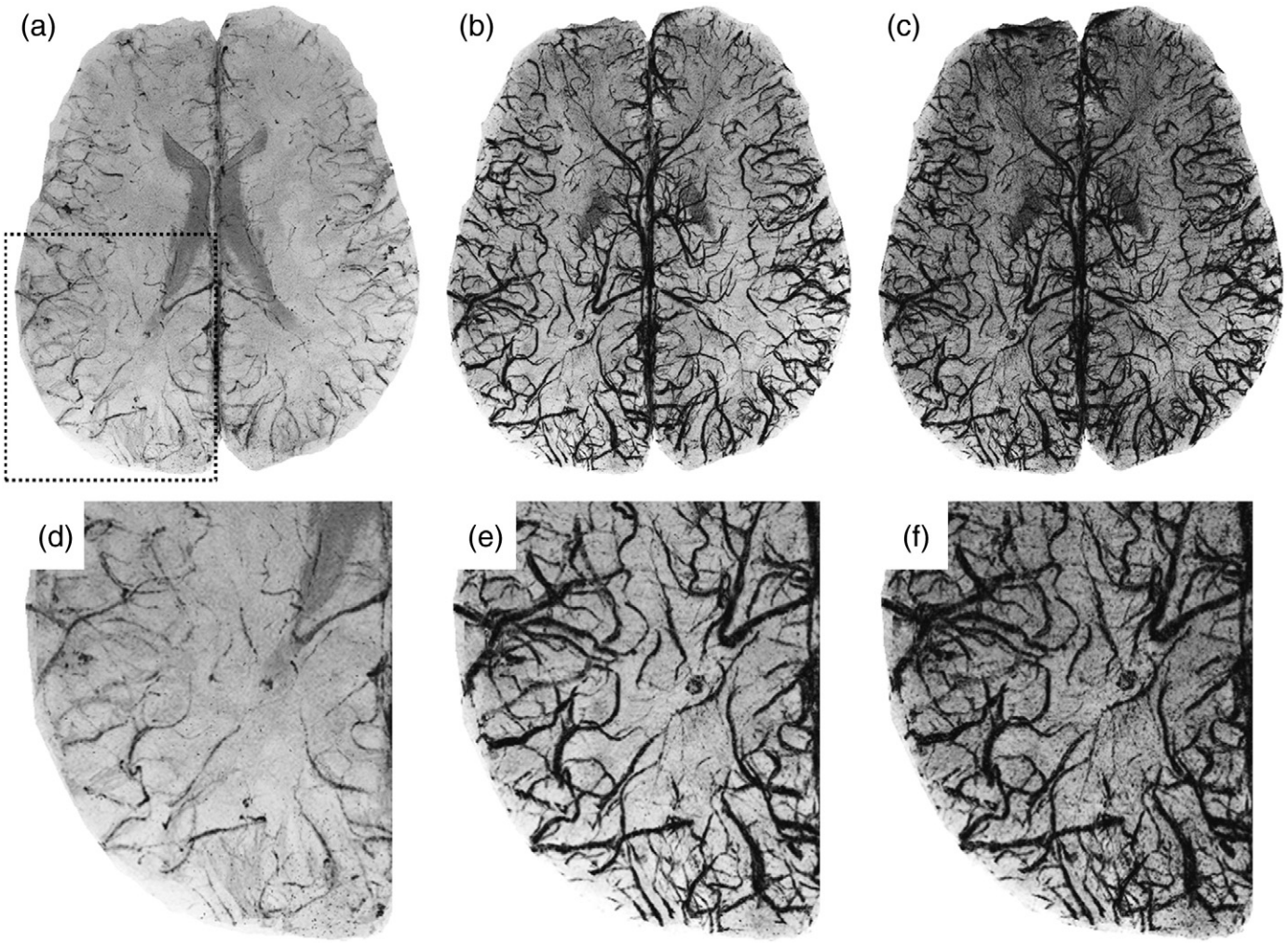

Fig. 9. Multiple contrast denoised SW venographies obtained using the two model-based method at TE = 11.18 ms (a), 27.71 ms (b), and 44.24 ms (c). Magnified views of the boxed area are shown in (d–f), respectively.

reconstructed images obtained by a time-resolved view-shared sequence (Wilman and Riederer, 1996) during dynamic contrast-enhanced MR angiography. A temporal footprint can also be understood as how fast the k-space data is acquired at a specific TE. The pixel bandwidths of GRE and MGRE sequences in the present study were 80 Hz/Px and 444 Hz/Px, respectively. Therefore, the GRE sequence required a 5.55-fold longer readout duration than the MGRE sequence. Due to this longer readout duration, the data acquired from the GRE sequence had a higher SNR than the MGRE sequence (before denoising), but its temporal footprint was higher, resulting in less temporal fidelity at a specific TE. Our proposed method used the data acquired by the MGRE sequence with a shorter temporal footprint. The low SNR of the data was compensated for by performing model-based denoising of both magnitude and phase data, resulting in a higher SNR than that of GRE imaging. Therefore, SW venographies obtained using our proposed method have higher SNR, CNR, and temporal fidelity than venographies obtained using conventional GRE imaging. The model-based denoising process had a negligible effect on the temporal footprint of the original data because the original decay signals changed slowly, following an exponential decay pattern. Thus, no sharp edges or boundaries were lost during the denoising process.

In conclusion, we demonstrated that high-resolution and high-SNR multiple-contrast SW venographies can be obtained by multi-echo MR acquisition and effective denoising methods based on a T_2^* relaxation model for the magnitude data and a linear phase model for the phase data in the temporal domain.

Acknowledgments

This work was supported by Basic Science Research Program through the National Research Foundation of Korea (NRF) funded by the Ministry of Education, Science and Technology (2011-0025574) and by the Korean government (MEST) (2012-009903).

References

Abdi, H., 2003. Partial least squares (PLS) regression. In: Lewis-Beck, M., Bryman, A., Futing, T. (Eds.), Encyclopedia for Research Methods for the Social Sciences. Sage, pp. 792–795.

Andrews, T., Lancaster, J.L., Dodd, S., Contreras-Sesvold, C., Fox, P.T., 2005. Testing the three-pool white matter model adapted for use with T_2 relaxometry. Magn. Reson. Med. 54, 449–454.

Berne, R.M., Levy, M.N., 1988. The circuitry, Physiology, 2nd edition. St. Louis, Mosby, pp. 395–397.

Dudink, J., Lequin, M., Weisglas-Kuperus, N., Conneman, N., Goudoever, J.B.V., Govaert, P., 2008. Venous subtypes of preterm periventricular haemorrhagic infarction. Arch. Dis. Child. Fetal Neonatal Ed. 93, 201–206.

Fan, J., Gijbels, I., 1996. Local Polynomial Modelling and Its Applications. Chapman & Hall, New York.

Gerig, G., Kubler, O., Kikinis, R., Jolesz, F., 1992. Nonlinear anisotropic filtering of MRI data. IEEE Trans. Med. Imaging 11, 221–231.

Griswold, M.A., Jakob, P.M., Heidemann, R.M., Nittka, M., Jellus, V., Wang, J., Kiefer, B., Haase, A., 2002. Generalized autocalibrating partially parallel acquisitions (GRAPPA). Magn. Reson. Med. 47, 1202–1210.

Haacke, E.M., Xu, Y., Cheng, Y.C.N., Reichenbach, J.R., 2004. Susceptibility weighted imaging (SWI). Magn. Reson. Med. 52, 612–618.

Haacke, E.M., Mittal, S., Wu, Z., Neelavalli, J., Cheng, Y.C.N., 2009. Susceptibility-weighted imaging: technical aspects and clinical applications, Part 1. Am. J. Neuroradiol. 30, 19–30.

Haider, C.R., Hu, H.H., Campeau, N.G., Huston III, J., Riederer, S.J., 2008. 3D high temporal and spatial resolution contrast-enhanced MR angiography of the whole brain. Magn. Reson. Med. 60, 749–760.

Hernando, D., Vigen, K.K., Shimakawa, A., Reeder, S.B., 2012. R_2* mapping in the presence of macroscopic B0 field variations. Magn. Reson. Med. 68, 830–840.

Hoogenraad, F.G.C., Reichenbach, J.R., Haacke, E.M., Lai, S., Kuppusamy, K., Sprenger, M., 1998. *In vivo* measurement of changes in venous blood-oxygenation with high resolution functional MRI at 0.95 Tesla by measuring changes in susceptibility and velocity. Magn. Reson. Med. 39, 97–107.

Hwang, D.S., Du, Y.P., 2009. Improved myelin water quantification using spatially regularized non-negative least squares algorithm. J. Magn. Reson. Imaging 30, 203–208.

Hwang, D., Kim, D.H., Du, Y.P., 2010. *In vivo* multi-slice mapping of myelin water content using T2* decay. NeuroImage 52, 198–204.

Jang, U., Hwang, D., 2011. High-quality Venography from Multi-echo MR Dataset Using T_2* Relaxation Model, 19. ISMRM, Montreal, Canada, p. 1292.

Jang, U., Hwang, D., 2012. High-quality multiple T_2(*) contrast MR images from low-quality multi-echo images using temporal-domain denoising methods. Med. Phys. 39, 468–474.

Jin, Z., Xia, L., Du, Y.P., 2008. Reduction of artifacts in susceptibility-weighted MR venography of the brain. J. Magn. Reson. Imaging 28, 327–333.

Kiselev, V.G., Posse, S., 1999. Analytical model of susceptibility-induced MR signal dephasing: effect of diffusion in a microvascular network. Magn. Reson. Med. 41, 499–509.

Lancaster, J.L., Andrews, T., Hardies, L.J., Dodd, S., Fox, P.T., 2003. Three-pool model of white matter. J. Magn. Reson. Imaging 17, 1–10.

Lawson, C.L., Hanson, R.J., 1974. Solving Least Squares Problems. Prentice-Hall, Englewood Cliffs, New Jersey.

Ogawa, S., Lee, T.M., Nayak, A.S., Glynn, P., 1990. Oxygenation-sensitive contrast in magnetic resonance image of rodent brain at high magnetic fields. Magn. Reson. Med. 14, 68–78.

Pawlik, G., Rackl, A., Bing, R.J., 1981. Quantitative capillary topography and blood flow in the cerebral cortex of cats: an in-vivo microscopic study. Brain Res. 208, 35–38.

Potchen, E., Haacke, E.M., Siebert, J.E., Gottshalk, A., 1993. Magnetic Resonance Angiography: Concepts and Applications. St Louis, Mosby.

Provencher, S.W., 1982. A constrained regularization method for inverting data represented by linear algebraic or integral equations. Comput. Phys. Commun. 27, 213–227.

Reichenbach, J.R., Venkatesan, R., Schillinger, D.J., Kido, D.K., Haacke, E.M., 1997. Small vessels in the human brain: MR venography with deoxyhemoglobin as an intrinsic contrast agent. Radiology 204, 272–277.

Reichenbach, J.R., Barth, M., Haacke, E.M., Klarhöfer, M., Kaiser, W.A., Moser, E., 2000. High-resolution MR venography at 3.0 Tesla. J. Comput. Assist. Tomogr. 24, 949–957.

Rodallec, M.H., Krainik, A., Feydy, A., Hélias, A., Colombani, J.M., Jullès, M.C., Marteau, V., Zins, M., 2006. Cerebral venous thrombosis and multidetector CT angiography: tips and tricks. RadioGraphics 26, 5–18.

Samsonov, A.A., Johnson, C.R., 2004. Noise-adaptive nonlinear diffusion filtering of MR images with spatially varying noise levels. Magn. Reson. Med. 52, 798–806.

Valentine, H.L., Does, M.D., Marshall, V., Tonkin, E.G., Valentine, W.M., 2007. Multicomponent T_2 analysis of dithiocarbamate-mediated peripheral nerve demyelination. Neurotoxicology 28, 645–654.

Wachowicz, K., Snyder, R.E., 2002. Assignment of the T_2 components of amphibian peripheral nerve to their microanatomical compartments. Magn. Reson. Med. 47, 239–245.

Wilman, A.H., Riederer, S.J., 1996. Improved centric phase encoding orders for three-dimensional magnetization-prepared MR angiography. Magn. Reson. Med. 36, 384–392.

Wink, A.M., Roderick, J.B., 2004. Denoising functional MR images: a comparison of wavelet denoising and Gaussian smoothing. IEEE Trans. Med. Imaging 23, 374–387.

Woolsey, T.A., Hanaway, J., Gado, M.H., 2008. The Brain Atlas: A Visual Guide to the Human Central Nervous System, third edition. John Wily & Sons, Inc.

Xu, Y., Haacke, E.M., 2006. The role of the voxel aspect ratio in determining apparent vascular phase behavior in susceptibility weighted imaging. Magn. Reson. Imaging 24, 155–160.

Ying, K., Clymer, B.D., Schmalbrock, P., 1996. Adaptive filtering for high resolution magnetic resonance images. J. Magn. Reson. Imaging 6, 367–377.